Acta Crystallographica Section D
Biological Crystallography
ISSN 0907-4449

Cloning, sequence and crystallographic structure of recombinant iron superoxide dismutase from *Pseudomonas ovalis*

Christopher J. Bond,[a,b] Jie-yu Huang,[b] Robin Hajduk,[b] Karen E. Flick,[b] Patrick J. Heath[b] and Barry L. Stoddard[b]*

[a]Program in Biomolecular Structure and Design, University of Washington, USA, and [b]Fred Hutchinson Cancer Research Center Program in Structural Biology, Division of Basic Sciences A3-023, 1100 Fairview Avenue North, Seattle WA 98109, USA

Correspondence e-mail: bstoddar@fhcrc.org

Received 14 March 2000
Accepted 3 July 2000

PDB Reference: *P. ovalis* iron superoxide dismutase, 1dt0.

The gene encoding the iron-dependent superoxide dismutase from *Pseudomonas ovalis* was cloned from a genomic library and sequenced. The ORF differs from the previously published protein sequence, which was used for the original structure determination, at 16 positions. The differences include three additional inserted residues, one deleted residue and 12 point substitutions. The gene was subcloned and the recombinant protein overexpressed, purified and crystallized in a trigonal space group. The structure was determined by molecular replacement and was refined to 2.1 Å resolution.

1. Introduction

Respiration is accompanied by the intracellular accumulation of low concentrations of reactive reduced oxygen species, such as superoxide anion ($O_2^{\cdot-}$). These species represent escaped intermediates in the four-electron reduction of oxygen. Under physiological conditions in the cell, $O_2^{\cdot-}$ decays through several mechanisms, including protonation to produce the hydroperoxyl radical, dismutation to produce O_2 and H_2O_2, and a Fenton reaction to produce the hydroxyl radical. All of these species, in addition to superoxide itself, react with a variety of molecular targets in the cell and cause oxidative damage that can lead to genetic mutation and/or cell death.

Organisms have developed an assortment of direct and indirect mechanisms to protect their cellular machinery against oxidative damage. A large number of small biological molecules, such as vitamin E, ascorbic acid and glutathione, have been shown to interact with free radicals and possess antioxidant and anticarcinogenic properties (Terao & Matsushita, 1988). Many enzymes catalyze the repair of damaged molecules. Finally, several catalysts have evolved that constitute a cell's primary antioxidant defenses. These enzymes include catalase, glutathione peroxidase and superoxide dismutase (SOD), which act in concert to convert reactive oxygen species into less toxic molecules.

Superoxide dismutase catalyzes the cyclic oxidation and reduction of the superoxide radical into oxygen and peroxide (McCord & Fridovich, 1969). SOD is induced in a variety of eukaryotic tissue sources by exposure of the organism to hyperbaric oxygen, as well as in the cytoplasm of most, if not all, aerobic prokaryotes (Fridovich, 1975). It has since been shown that the absence of SOD creates a conditional sensitivity to oxygen (Carlioz & Touati, 1986) and that temperature-sensitive mutations in bacterial SOD produce a strain with parallel defects in their tolerance for oxygen (McCord, 1973). There are four known SOD catalysts: an copper/zinc glycoprotein (Cu/ZnSOD) found in the extracellular fluids of many eukaryotes (Marklund *et al.*, 1982), a

cytosolic copper/zinc enzyme found primarily in eukaryotic tissues and manganese- and iron-specific enzymes (MnSOD, FeSOD) which are ubiquitous and represent the major source of SOD activity in most fungi, prokaryotes, mitochondria and blue–green algae (Valentine & Pantoliano, 1981; Keele *et al.*, 1970; Asada *et al.*, 1975). MnSOD and FeSOD are homologues of each other, but are unrelated to Cu/ZnSOD. The SOD family of enzymes are reviewed in Fridovich (1995).

Iron and manganese superoxide dismutases are usually found as dimers or tetramers composed of identical subunits of approximately 200 residues. One metal ion is bound per subunit. The Fe- and Mn-dependent enzymes are extremely specific both for superoxide anion as substrate as well as for a specific metal ion in their respective active sites. Substitution of alternate metal species usually yields inactive enzyme (Ose & Fridovich, 1976; Yamakura & Suzuki, 1980). Several investigations into the metal specificity of either MnSODs or FeSODs have focused on the role of residue 143, which is either Gln or His in all homologous SODs (Hsieh *et al.*, 1998, Bunting *et al.*, 1998). Mutation of the equivalent residue His145 in a FeSOD from *Mycobacterium tuberculosis* to Glu affects the preferential specificity for iron (Bunting *et al.*, 1998). Atomic absorption spectra and peroxide inhibition experiments indicate that the His145Glu mutant binds Mn, while the active-site metal is iron in both the wild-type enzyme and a conservative mutant His145Gln (Bunting *et al.*, 1998). Recent studies have shown a pH dependence for metal-ion specificity in MnSOD from *Serratia marcescens* (Yamakura *et al.*, 1995).

The active sites of FeSOD and MnSOD display conserved metal-binding residues and active-site structures, including similar shells of aromatic residues that surround the active-site metal and its ligands. In previous work, the 2.1 Å crystal structure of wild-type iron superoxide dismutase from *P. ovalis* was determined (Stoddard, Howell *et al.* 1990). The structure determination relied on non-recombinant enzyme purified from *Pseudomonas* cell paste and a published sequence determined from direct protein-sequencing methods reported by a separate group (Isobe *et al.*, 1987). The study was hampered by the crystals used in the analysis, which exhibited significant disorder and twinning, as well as the available sequence, which contained multiple errors as demonstrated in this paper. The twinning within these crystals was physically observable under polarized light and manifested itself in split peak profiles when data was collected. In order to improve the quality of the structure, as well as to pursue site-directed mutagenesis and mechanistic studies, the gene encoding the enzyme has been cloned directly from a *Pseudomonas* chromosomal library, sequenced and subcloned for protein expression and crystallographic studies. The resulting crystals of recombinant FeSOD, which belong to a new space group (see §2), uniformly extinguish polarized light and give excellent peak profiles and data-processing statistics. This paper reports the corrected sequence of the enzyme, the purification and crystallization of the recombinant protein and the high-resolution crystal structure of the recombinant wild-type enzyme in a new space group.

2. Material and methods

2.1. Cloning and sequencing

A *P. ovalis* chromosomal plasmid library was constructed in pUC19 and amplified. The library, with insert size 7–9 kbp, was constructed by partial digest of *P. ovalis* chromosomal DNA with the restriction enzyme *Sph*I and subsequent ligation of the purified DNA product into the plasmid vector. The size of the library was about 15 000 unique recombinants. The library was amplified and plasmid stocks were prepared by alkaline lysis and CsCl centrifugation. Degenerate oligonucleotide primers corresponding to two separate conserved tryptophan-rich regions of FeSOD were designed on the basis of the published protein sequence and used for PCR amplification of a 350 base-pair DNA fragment encoding the partial FeSOD gene. The sequence of the primers were 5′-TGGAANCA-NACTTNTANTGGAA-3′ (N-terminal, corresponding to the published protein sequence W_{75}NHTFYWN_{82}) and 5′-CGGGT-NAANTGNTNNAAGGTNTT-3′ (C-terminal, corresponding to the reverse sequence A_{190}WNVLNWF_{183}). PCR products of the correct size were separated from other PCR products by agarose electrophoresis, purified and subcloned into a pSL1180 plasmid (Pharmacia) for sequence analysis using *Bam*HI restriction sites engineered into the PCR primers, which are complementary to cloning sites in the plasmid polylinker.

The resulting inserts were sequenced across both DNA strands. Sequencing was performed on an Applied Biosystems model 377 DNA sequencer using a fluorescent *Taq* dye-terminator system. The final sequencing data was confirmed by additional runs with overlapping primers across any regions that gave unclear or ambiguous output. An individual clone of the partial FeSOD reading frame was amplified, end-labelled and used for hybridization screening of the original chromosomal genomic library. A clone containing the intact full-length ORF was identified and the gene was resequenced as described above, using both strands as templates and overlapping sequencing runs. The genomic sequence for the *P. ovalis* FeSOD gene is shown in Fig. 1.

2.2. Subcloning, expression and purification

The full-length ORF encoding FeSOD was subcloned into the pTrc99A plasmid vector (Pharmacia) and the resulting vector was transformed into the *Escherichia coli* strain QC774 [φ(sodA-lacZ)49 φ(sodB-kan)1-Δ2 *Cm*^{r}Km^r]*B*, a host system constructed and provided by Carlioz and Touati, in which the chromosomal copies of the genes encoding FeSOD or MnSOD are disrupted by insertion of Mu transposons (Carlioz & Touati, 1986). This strain was used both to demonstrate that the cloned SOD gene rescues cell growth on Paraquat and also for protein expression against an SOD-null background. The protein was overexpressed in this strain in rich L-Broth after IPTG induction.

The cells were grown to an absorbance of 0.6 OD_{600}. Protein expression was then induced by addition of IPTG to a final concentration of 0.1 m*M*. The cells were grown at 310 K for 4 h and then harvested by centrifugation. The cell pellet was

resuspended in cold isotonic buffer (50 m*M* Tris pH 7.5, 150 m*M* NaCl, 2 m*M* EDTA). The cells were pelleted and resuspended in 50 m*M* Tris pH 6.7. Lysozyme was added to 200 µg ml^{-1} and the cells were incubated on ice for 10 min. The cells were lysed by sonication and then centrifuged. The supernatant was transferred to a clean vessel. Ammonium sulfate was added to a final concentration of 55% saturation and precipitated protein was pelleted by centrifugation and discarded. Ammonium sulfate was added to the supernatant to a final concentration of 85% saturation and the protein was harvested by centrifugation. The protein pellet (which represents almost pure FeSOD) was redissolved in 50 m*M* Tris pH 6.7 and loaded onto a POROS HQ 50 column. The column was washed with 50 m*M* Tri pH 6.7 until the absorbance at 280 nm reached 10% of the maximum absorbance while loading the protein. FeSOD was then eluted from the column as a single peak by an increasing gradient (0–300 m*M*) of KCl and was concentrated to 40 mg ml^{-1} with a Centricon 10.

2.3. Crystallization and structure determination

FeSOD was diluted to 9 mg ml^{-1} with 100 m*M* Tris pH 8.0. Crystals were grown at room temperature using the hanging-drop vapor-diffusion method against reservoirs of 2.0–2.6 *M* ammonium sulfate buffered at pH 8.0 with 100 m*M* Tris. Crystals appear within 3 d and under optimal conditions grow to dimensions of approximately 1.2 × 0.4 × 0.4 mm. The crystals were either mounted in quartz capillaries for room-temperature data collection or flash-cooled for data collection under a nitrogen cryostream by sequential transfer to solutions containing 3.0 *M* ammonium sulfate and an increasing amount of glycerol, ranging from 10%(*v*/*v*) to a final concentration of 30%(*v*/*v*).

Data were collected on a Rigaku R-AXIS IV area detector mounted on a Rigaku RU-200 rotating-anode X-ray generator equipped with Yale focusing mirrors (Molecular Structure Corporation). All reflections were reduced using the *DENZO*/*SCALEPACK* crystallographic data-reduction package (Otwinowski & Minor, 1997). During data processing, the crystals were found to exhibit trigonal symmetry and belong to space group $P3_221$, with unit-cell parameters $a = b = 117$, $c = 83$ Å. The unit-cell parameters decrease by 2 Å in *a* and *b* as a result of flash-cooling, giving dimensions of 115 Å, while *c* was unchanged at 83 Å. These crystals are greatly improved over the original crystals of non-recombinant protein, with no observable twinning and low mosaicity (less than 0.4°). In comparison, the original crystals of non-recombinant protein failed to uniformly extinguish plane-polarized light, gave non-uniform peak profiles during data collection and produced data that failed to converge during refinement (see below). There are three monomers in each asymmetric unit (V_M = 2.5 Å^3 Da^{-1}; solvent content = 46%). Two data sets were collected, one at 298 K and one at 98 K. The room-temperature data set was 95% complete to 2.1 Å resolution, with an overall R_{merge} of 3.9%; the low-temperature data set was 98% complete to 2.1 Å resolution, with an overall R_{merge} of 4.8%. Table 1 gives the data-collection statistics.

The structure of recombinant *P. ovalis* superoxide dismutase in the trigonal space group was solved by molecular replacement, using the cryo-cooled data set for the initial experiment. The structure of *E. coli* Fe^{II} superoxide dismutase (Lah *et al.*, 1995) was used as the search model in the molecular-replacement program *EPMR* (Kissinger & Gehlhaar, 1997). Three independent solutions were found in the asymmetric unit using a monomer as a search model (correlation coefficients 0.44, 0.48 and 0.55). All three monomeric solutions were combined and subjected to rigid-body refinement using *X-PLOR* (Brünger, 1993). The resulting solution had an *R* factor of 55%. During the initial rounds of refinement, non-crystallographic symmetry (NCS) was imposed on all three subunits using restraints of 1670 kJ mol^{-1} for backbone and side-chain atoms. The resulting solution was put through a round of simulated annealing using an initial temperature of 3000 K and NCS restraints of 630 kJ mol^{-1} for the backbone

```
1   2   3   4   5   6   7   8   9   10  11  12  13  14  15  16  17  18
ATG GCT TTT GAA TTG CCA CCG CTG CCG TAC GCC CAC GAT GCC CTG CAG CCG CAC
Met-Ala-Phe-Glu-Leu-Pro-Pro-Leu-Pro-Tyr-Ala-His-Asp-Ala-Leu-Gln-Pro-His

19  20  21  22  23  24  25  26  27  28  29  30  31  32  33  34  35  36
ATC TCC AAG GAA ACC CTG GAG TTT CAC CAC GAC AAG CAC CAC AAC ACC TAT GTC
Ile-Ser-Lys-Glu-Thr-Leu-Glu-Phe-His-His-Asp-Lys-His-His-Asn-Thr-Tyr-Val
                          (Tyr)

37  38  39  40  41  42  43  44  45  46  47  48  49  50  51  52  53  54
GTG AAC CTG AAC AAC CTG GTC CCA GGC ACC GAA TTC GAA GGC AAG ACC CTG GAA
Val-Asn-Leu-Asn-Asn-Leu-Val-Pro-Gly-Thr-Glu-Phe-Glu-Gly-Lys-Thr-Leu-Glu
                                  (Thr-Pro-Glu)

55  56  57  58  59  60  61  62  63  64  65  66  67  68  69  70  71  72
GAG ATC GTC AAG ACC TCT TCG GGC GGC ATC TTC AAC AAC GCC GCT CAG GTC TGG
Glu-Ile-Val-Lys-Thr-Ser-Ser-Gly-Gly-Ile-Phe-Asn-Asn-Ala-Ala-Gln-Val-Trp
              (Ser)

73  74  75  76  77  78  79  80  81  82  83  84  85  86  87  88  89  90
AAC CAC ACC TTC TAC TGG AAC TGC CTG GCG CCA AAC GCC GGT GGT CAA CCG ACC
Asn-His-Thr-Phe-Tyr-Trp-Asn-Cys-Leu-Ala-Pro-Asn-Ala-Gly-Gly-Gln-Pro-Thr
                                (Ser)   (Asp-Gly)

91  92  93  94  95  96  97  98  99  100 101 102 103 104 105 106 107 108
GGT GCC CTG GCT GAC GCC ATC AAC GCC GCT TTC GGG TCC TTC GAC AAG TTC AAG
Gly-Ala-Leu-Ala-Asp-Ala-Ile-Asn-Ala-Ala-Phe-Gly-Ser-Phe-Asp-Lys-Phe-Lys

109 110 111 112 113 114 115 116 117 118 119 120 121 122 123 124 125 126
GAA GAG TTC ACC AAG ACT TCG GTT GGT ACC TTC GGT TCC GAC TGG GGC TGG CTG
Glu-Glu-Phe-Thr-Lys-Thr-Ser-Val-Gly-Thr-Phe-Gly-Ser-Gly-Trp-Gly-Trp-Leu
                                                              (Ala)

127 128 129 130 131 132 133 134 135 136 137 138 139 140 141 142 143 144
GTG AAG AAA GCT GAC GGT TCC CTG GCC CTG GCC AGC ACC ATC GGC GCC GGT TGC
Val-Lys-Lys-Ala-Asp-Gly-Ser-Leu-Ala-Leu-Ala-Ser-Thr-Ile-Gly-Ala-Gly-Cys
   (Lys --- Ala)                    (Cys)                          (Ala)

145 146 147 148 149 150 151 152 153 154 155 156 157 158 159 160 161 162
CCG CTG ACC ATC GGC GAC ACC CCG CTG CTG ACC TGC GAC GTC TGG GAA CAC GCC
Pro-Leu-Thr-Ile-Gly-Asp-Thr-Pro-Leu-Leu-Thr-Cys-Asp-Val-Trp-Glu-His-Ala
          (Ser)

163 164 165 166 167 168 169 170 171 172 173 174 175 176 177 178 179 180
TAC TAC ATC GAC TAC CGC AAT CTG CGT CCG AAG TAC GTC GAG GCG TTC TGG AAC
Tyr-Tyr-Ile-Asp-Tyr-Arg-Asn-Leu-Arg-Pro-Lys-Tyr-Val-Glu-Ala-Phe-Trp-Asn

181 182 183 184 185 186 187 188 189 190 191 192 193 194 195 196 197 198
CTG GTC AAC TGG GCC TTC GTT GCC GAA CAG TTC GAA GGC AAG ACC TAC AAG GTC
Leu-Val-Asn-Trp-Ala-Phe-Val-Ala-Glu-Gln-Phe-Glu-Gly-Lys-Thr-Tyr-Lys-Val
                                (Glu --- ---)           (Phe)   (Ala)

200
TGA
 *
```

Figure 1
Nucleotide sequence for *P. ovalis* FeSOD. Shown below the nucleotide sequence is the translated protein sequence used for the structure determination of the recombinant protein. Shown underneath in parentheses are positions in the original reported protein sequence (Stoddard *et al.*, 1990) that deviate from the translated genomic sequence. As described in the text, there are 16 changes, including one deletion (of a proline between Thr46 and Glu47), three insertions (of Lys129, Phe191 and Glu192) and 12 point substitutions.

Table 1
Data and refinement summary.

	Ambient	Cryo-cooled
Temperature (K)	298	98
Space group	$P3_221$	$P3_221$
Unit-cell parameters (Å)	117 × 117 × 83	115 × 115 × 83
Total No. of reflections	36878	36255
Reflections used for R_{free}	1865	1837
$\langle I/\sigma(I)\rangle$	15.1	14.4
d_{min} (Å)	2.1	2.1
R_{merge} (%)	3.9	4.8
Completeness (%)	95.3	97.6
No. of protein atoms	4614	4614
No. of water molecules	113	189
R_{cryst} (%)	21	22
R_{free} (%)	26	29
Average B value (Å^2)		
Main chain	32.19 (1.16)	29.96 (0.67)
Side chain	33.01 (1.16)	29.52 (0.67)
Ramachandran plot		
Core (%)	91.6	90.4
Allowed (%)	7.2	8.4
Generously allowed (%)	1.2	1.2
Disallowed (%)	0.0	0.0
R.m.s. deviation		
Bonds (Å)	0.005	0.009
Angles (°)	1.15	1.30
Dihedral angles (°)	24.8	25.1

and 42 kJ mol^{-1} for the side chains and a single B factor of 20 Å^2. These B factors were then individually refined. Once R_{free} dropped to 33%, the working reflection set was scaled using a bulk-solvent correction. Electron-density maps, using Fourier coefficients corresponding to both $F_o - F_c$ and $2F_o - F_c$, were calculated for a stage of manual rebuilding. Solvent peaks were then picked using the $F_o - F_c$ difference map calculated using the rebuilt model. The solvated protein model was then put through a second round of refinement, including individual B factors. At this point, water atoms with refined B factors greater than 50 Å^2 were removed. The final model was then subjected to an additional round of solvent flattening followed by a 40-step conjugate-gradient minimization. The final model has a working R factor of 22% for all recorded data to 2.1 Å resolution and a free R factor of 29%. Although the working R factor is only 2% lower than that reported for the original structure, the free R factor is significantly lower (by 8%) than the same statistic (calculated in retrospect) for the earlier structure. In addition, the root-mean-square (r.m.s.) deviations from ideal bond lengths, angles and dihedral angles are much lower (0.009 Å, 1.3° and 25.1°, respectively) than the equivalent values for the original structure. There are no Ramachandran outliers observed in the final model.

The structure of FeSOD at room temperature was also solved and refined, using the previously refined structure as an initial model and a similar refinement protocol to that described above. The final refinement statistics for this structure display slightly improved values for the R_{cryst} and R_{free} (21 and 26%, respectively) and for the protein geometry. This reflects the stronger data collected under these conditions. Table 1 presents refinement statistics for both structures, including the number of atoms and average B values.

3. Results and discussion

3.1. Differences between translated nucleotide sequence and original protein sequence

There are 16 differences between the previously published amino-acid sequence of *P. ovalis* FeSOD and the translated protein sequence presented here (Fig. 1). These sequence differences are distributed throughout the tertiary structure of FeSOD (Fig. 2, Table 2). 12 of these differences are point substitutions, three are insertions of one or two residues and one is a deletion of a single residue. Five of these changes are in the C-terminal ten residues of the protein and six are in surface loops. Four point substitutions are found in regions of secondary structure: two in α-helices and two in β-strands. No changes were made in the active site or among the catalytic residues. The substitution of phenylalanine for tyrosine at residue 26 is closest to the active site; this point substitution is 8.2 Å away from the catalytic iron. Nine of the sequence changes are at positions buried within the protein and eight are on the surface. One residue is changed at the dimer interface. No systematic trends are obvious in the pattern of sequence changes at the level of either the monomer or the dimer.

3.2. Differences in refined X-ray structures

The structure and architecture of FeSOD has been described in detail elsewhere (Stoddard *et al.*, 1990). Briefly, FeSOD is a homodimer of two subunits. Each monomer is primarily α-helical, with a single three-stranded β-sheet near the C-terminus of the protein (Fig. 2). The $O_2^{\cdot-}$-binding site is at the apex of a large funnel-shaped cleft formed at the dimer interface (Lah *et al.*, 1995; Stoddard, Ringe *et al.*, 1990). The

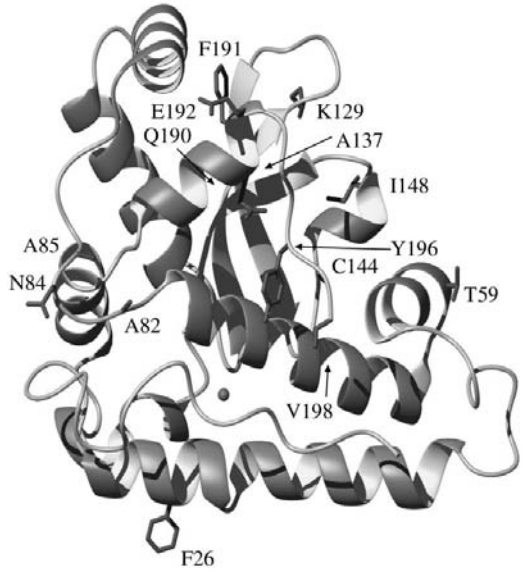

Figure 2
Structure of an SOD monomer. Side chains are shown where the sequence of the protein deviates from the original model. The N-terminal Met is not observed in the electron-density maps.

Table 2
Sequence changes in *P. ovalis* FeSOD.

Residue numbering is of the sequence reported here. C^{α} distances for each insertion or mutation to the active-site iron are given.

Residue	Isobe *et al.* (1987)	Gene sequence	Distance to iron (Å)
26	Tyr	Phe	9.6
46	Pro	—	—
59	Ser	Thr	21.7
82	Ser	Glu	16.3
84	Asp	Asn	22.3
85	Gly	Ala	22.0
124	Ala	Gly	11.6
129	—	Lys	24.1
137	Cys	Ala	16.8
144	Ala	Cys	12.8
148	Ser	Ile	20.7
190	Glu	Gln	20.7
191	—	Phe	23.1
192	—	Glu	26.0
196	Phe	Tyr	18.2
198	Ala	Val	—

cleft is approximately 10 Å wide and 14 Å deep. Residues from each subunit form the upper edge of the cleft. The $O_2^{\cdot-}$-binding site is located directly above the catalytic Fe atom, is approximately 3.6 Å in diameter and is lined primarily by aromatic residues.

Overall, the structure presented here is only slightly different from that previously determined. There are no changes in connectivity or in the register of side chains across secondary-structural elements. The C^{α} r.m.s. deviation of conserved structural elements (helices 1–6 and the central β-sheet) between the two structures is 1.1 Å. The C^{α} r.m.s.d. of the residues involved in iron ligation is 0.26 Å. The main differences in backbone structure are in two loops. Residues in the first loop N-terminal to α_1 have swung in toward the main body of the protein. In particular, the r.m.s. deviation for the backbone atoms of Ala13 and Leu14 is 4.9 Å. In a similar manner, the loop (residues 129–132) between β_1 and β_2 is displaced from its position in the previous structure. This displacement results in a backbone r.m.s. deviation for residues Asp130–Ser132 of 3.71 Å between the two structures.

The sequence changes described above, along with the new crystal form, result in mostly small differences between the structure presented here and that reported earlier. Only two regions of the protein structure are significantly affected by these changes. The first is the modelling and refinement of a canonical α-helix between residues Leu53 and Thr59. This region was previously modelled in a 'near-helical' conformation. The point change Ser59Thr is at the C-terminus of this new helix. The side-chain hydroxyl H atom of Thr59 forms a hydrogen bond with the main-chain carboxyl O atom of Glu54, which appears to stabilize the helix. A second significant change is found at the C-terminal end of the protein, which is well ordered in the new crystal form. As a result, there are nine additional residues (191–198) modelled in this structure. These residues pack against residues from strands β_1 and β_3 as well as the loop between helices α_3 and α_4, burying approximately 1100 $Å^2$ of previously exposed structure.

Neither the insertion of Lys129 or the deletion of Pro47 significantly affect the architecture of the protein. Lys129 forms the N-terminal end of the β_2 turn. In the new structure, the insertion of Lys129 extends the turn by one residue, resulting in a β-sheet which remains in register with that of the previous structure. Pro46 in the earlier model is in a large loop C-terminal to helix α_1. The deletion of this residue has little effect: the ends of α_1 are in similar positions in both structures, as are residues 46–52. The net effect of ΔPro46 is to pull the solvent-exposed loop between Leu42 and Phe48 closer to the body of the protein, as illustrated by the 2.5 Å inward movement of Pro44 C.

In the previously solved structure the asymmetric unit contained one enzyme dimer. The asymmetric unit in the study presented here contained three SOD monomers consisting of one and a half enzyme dimers. The one unpaired monomer in the asymmetric unit makes a native dimeric interaction with a symmetry-related partner. This crystallographic dimer is formed by a twofold rotation across the *a* axis and a translation of $-1/3\ l$ along *c*. The all-atom r.m.s. deviation between the crystallographic and non-crystallographic dimers was 0.33 Å. Given the small differences between the crystallographic and NCS dimers, the following discussion will focus only on describing the NCS dimer interface.

The dimer interface of FeSOD is stabilized by approximately 104 pairwise atomic contacts, involving 20 residues from each subunit. Approximately 880 $Å^2$ of surface area is buried for each subunit in this interface. The majority of the atomic contacts in the interface are observed twice, with the symmetry-related side chains forming similar interactions. Any asymmetric interaction in the dimer interface deviates only slightly from its symmetry-related counterpart. For example, Phe26 makes five atomic contacts with the side-chain atoms of Arg167 in the second subunit. The contacts between residues 26 and 167′ include a packing interaction between Phe26 $C^{\varepsilon 2}$ and Arg167 C^{β}. In contrast, this particular contact is not observed between symmetry-related residues 26′ and 167. The dimer interface in the new crystallographic model is quite similar to the original model. Overall, the dimer interface is formed by the same residues as in the previous structure; however, the specific pairwise atomic interactions have changed slightly in the new structure. For example, Phe118 now interacts with residues 140′ and 141′, whereas in the previous structure Phe118 only contacted residue 141′. In comparison to the previous model, 17 of the unique atomic contacts are lost while ten new intersubunit contacts are made. Several of these changes are associated with an amino-acid sequence change. For example, in the previously published structure, Tyr26 makes several contacts with Tyr166′ in the adjoining subunit. This contact is lost in the new structure, where Tyr26 is replaced by a phenalanine.

3.3. Active-site geometry

The active-site metal ligands are identical to the previous structure. As a result of the sequence changes, the numbering

Table 3
Metal coordination geometry.

Values in parentheses for the *P. ovalis* structure are standard deviations for three independent enzyme monomers in the crystallographic asymmetric unit.

	P. ovalis SOD	*E. coli* Fe^{III} SOD
Bond lengths (Å)		
Fe—OD1 (Asp156)	1.9 (0.06)	2.2
Fe—N (His160)	2.0 (0.08)	2.1
Fe—N (His73)	2.1 (0.06)	1.9
Fe—N (His26)	2.2 (0.05)	2.1
$Fe—OH_2$	2.1 (0.02)	—
Average	2.1	2.1
Bond angles		
O(156)—Fe—N(73)	117.9 (2.7)	112.3
O(156)—Fe—N(160)	109.8 (2.8)	119.7
N(160)—Fe—N(73)	127.5 (5.4)	127.9
N(26)—Fe—N(73)	86.0 (1.7)	94.8
N(26)—Fe—N(160)	85.5 (0.3)	90.5
N(26)—Fe—O(156)	82.3 (0.8)	85.2
$N(26)—Fe—OH_2$	173.1 (2.5)	—

of one metal ligand (His74) is changed to His73. There are essentially only two significant differences between the active site of the previous model and that presented here. The side chain of Trp123 is coplanar with the old model, but is flipped within that plane. The second difference is observed for Tyr34, whose C^{α} is shifted by 1.6 Å. This shift results in an increase of 0.3 Å in the distance between the side-chain hydroxyl group of Tyr34 and the nearest side-chain atom of Gln69. We have modelled the Gln69 side chain with its amide N atom positioned to be a hydrogen-bond donor to Tyr34, in agreement with the structure of *E. coli* FeSOD. It is formally possible that this difference in the position of Tyr34 is the result of a difference in the protonation state of the side-chain hydroxyl group owing to the higher pH (8.0 compared with 4.8 for the original structure). However, this is a relatively minor change in the position of the hydroxyl O atom and is most likely not a consequence of changes in the protonation state of Tyr34. Additionally, the hydroxyl O atom of Tyr34 is in essentially in the same position as the equivalent hydroxyl group in the structure of FeSOD from *E. coli* (Lah *et al.*, 1995) solved at pH 7.0.

In the room-temperature model the iron is obviously pentacoordinate in all three independent monomers (Fig. 3). Four of the ligands are donated by the protein (His26, His73, His160 and Asp156) and a water acts as the fifth ligand. As with the previous model, the iron is coordinated in a trigonal bipyramidal geometry, with His26 and the water serving as axial ligands (Table 3). Residues His73, Asp156 and His160 are the planar ligands, with an average in-plane angle of 118°. The average through-iron angle connecting axial and planar ligands is 88°. These numbers are close to the ideal angles of 120° and 90° for a perfect trigonal bipyramid. The average ligand distance is now 2.1 Å. The orientation of the water is well suited to act as a fifth ligand (Table 3). The bound water has a *B* factor of 11.4 $Å^2$, which is fairly close to the temperature factors of both the iron (24.9 $Å^2$) and the other four ligands (average side-chain *B* factor = 16.0 $Å^2$). In all three subunits the Fe atoms refine to an occupancy of 1.0.

Three of the four protein ligands are stabilized by hydrogen-bonding interactions. The main-chain N atom of His26 participates in an $i \rightarrow i + 4$ helical hydrogen bond with the carbonyl C atom of Glu22. A water appears to mediate the stabilization of His26 $N^{\delta 2}$, with a distance between the side-chain N atom and the water O atom of 2.81 Å. His73 is also stabilized by hydrogen-bonding interactions. His73 N^{δ} is 2.53 Å from the side-chain O atom of Gln69 and an angle of 147.2° is made between Gln69 C—O and His73 N^{δ}. As reported earlier, His160 is stabilized *via* a hydrogen-bonding network which spans the dimer interface. The side-chain carboxyl group of Glu159 reaches across the dimer interface, forming a hydrogen bond to the His160 N^{δ} in the adjoining subunit; this side-chain contact directly links the two active-site histidines. His160 also interacts in a water-mediated main-chain hydrogen bond.

4. Conclusions

We present here the cloned FeSOD gene from *P. ovalis* and its corresponding crystallographic structure at 2.1 Å. The new structure is significantly improved over the earlier structure reported by Stoddard *et al.* (1990). 16 sequence corrections have been incorporated into the new structure. Most of these are single amino-acid point substitutions. None of these sequence changes cause a significant change to the overall structure of FeSOD, nor do they appear to alter prior conclusions regarding the catalytic mechanism and efficiency of this catalyst. The *R* factor has decreased by 2% (22 compared with 24%) and, more importantly, the overall geometric integrity was improved. Both bond length and angle r.m.s.d.s are significantly lower, as are the number of Ramachandran outliers. Furthermore, all the hallmark features of FeSOD active sites are preserved, including pentacoordinate metal ligation, trigonal bypyramidal ligation geometry and an axial water ligand.

The structural changes presented here which are most important to the catalytic mechanism of FeSOD are the adjustments to the refined metal-ligation geometry. Specifically, average ligand distances have decreased to 2.1 Å. The largest change in iron coordination was an inward movement of His26 toward the iron by 0.4 Å. Previously, the His26–iron distance was longer than expected for most iron ligands. The iron–His26 distance of 2.2 Å in the improved structure agrees well with an average distance of 2.19 Å from the other three holo-FeSOD structures. In addition to the four protein ligands, clear electron density was seen for water as the fifth ligand. Both the coordination position and water–iron bond length are similar to those in other FeSODs.

Seven FeSOD structures have been solved and deposited in the PDB (Stoddard, Howell *et al.*, 1990; Stoddard, Ringe *et al.*, 1990; Lah *et al.*, 1995, Cooper *et al.*, 1995; Stallings *et al.*, 1983; Schmidt *et al.*, 1996, 1998). All of these structures were determined by X-ray crystallography. Of the seven, three are azide-inhibited FeSOD structures (Lah *et al.*, 1995; Cooper *et*

al., 1995; Stoddard, Ringe *et al.*, 1990; Schmidt *et al.*, 1998). In all the holo-FeSOD structures the iron is pentacoordinate and in the majority of the structures this coordination is trigonal bipyramidal. In a recently reported structure of a cryo-trapped MnSOD, a hydroxide ion acted as a sixth ligand, coordinating the active-site Mn in a distorted octahedral geometry (Borgstahl *et al.*, 2000). One of the holo structures, an FeSOD from *M. tuberculosis*, has a distorted octahedral ligation geometry (Cooper *et al.*, 1995). However, this difference may be purely semantic, as the active sites from these two structures are very similar. Specifically, the average in-plane ligand angle is 119.7° in *M. tuberculosis*, compared with 118.4° in *P. ovalis*. Little change in active-site structure or iron coordination is manifested by changes in the redox state of the iron. Both ligand bond angles and distances for *E. coli* Fe^{III} SOD, *E. coli* Fe^{II} SOD (Lah *et al.*, 1995) and *P. ovalis* Fe^{III} SOD are nearly identical. In the structure presented here, the iron is most likely oxidized, as no specific measures were taken to maintain a reducing environment during crystallization and data collection.

The active sites of both monomers directly interact *via* a hydrogen-bond linkage. Glu159 from one chain forms a hydrogen bond with His160 of the opposing monomer. This transdimer interaction is preserved among all the FeSODs whose structures have been determined. It is unclear what if any effect this link has on catalysis, or if its sole importance is in dimer stabilization. The hydrogen-bond distance between Glu159 and His160 is not affected by oxidation, reduction or binding of inhibitor (Lah *et al.*, 1995; Stoddard, Ringe *et al.*, 1990). This argues against any communication between active sites regarding redox state or substrate binding. However, there have been no systematic investigations into the effects of transsubunit interactions on catalysis.

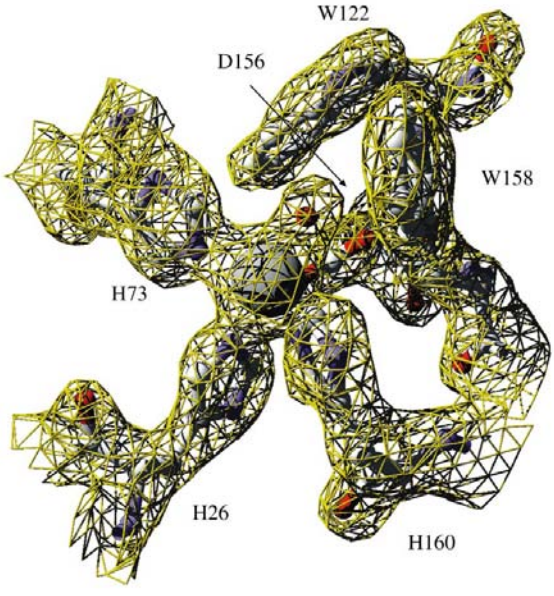

Figure 3
SOD active site and geometry. Density shown is for a $2F_o - F_c$ omit map contoured at 3σ. Direct coordination to the metal from protein side chains and a single solvent molecule are shown.

As has been previously noted, residues His30 and Tyr34 block access to the putative substrate-binding pocket (Sines *et al.*, 1990). This limited accessibility to the active site is also seen in the two azide-complexed FeSOD structures. It has been proposed that substrate binding must be accompanied by a transient conformational change involving movement of at least Tyr34 (Sines *et al.*, 1990) allowing access to the active site. It is unclear as yet whether substrate binding is facilitated by a specific conformational change or whether accessibility is linked to non-specific side-chain dynamics. We see no evidence of elevated dynamics for either His30 or Tyr34. The average side-chain temperature factors for residues 30 and 34 in the room-temperature structure is 23.7 (7.1) $Å^2$, compared with an overall temperature factor of 33.0 $Å^2$. Temperature factors for these residues are also low in the other published FeSOD structures. Thus, at least in the available crystal structures, His30 and Tyr34 are not in a dynamic equilibrium with multiple conformations. This however does not suffice as a proof of the second mechanism. Further support for this mechanism would require solution-state dynamic measurements. While the role of Tyr34 in substrate binding remains unclear, a large body of work supports a functional role for the side-chain hydroxyl group of Tyr34. Several studies indicate a functional role for the side-chain hydroxyl group of Tyr34. Substitution of Phe for Tyr34 in human mitochondrial manganese SOD increases enzyme stability but decreases k_{cat} by tenfold (Guan *et al.*, 1998). Additionally, the same mutation Tyr34Phe in FeSOD from *E. coli* eliminates the sensitivity to pH in active-site chemical shifts, implying the observed p*K* of 8.5 in Fe^{II} SOD is most likely a consequence of deprotonation of Tyr34 OH (Sorkin *et al.*, 1997; Sorkin & Miller, 1997).

BLS is funded for this work by the NIH (GM49857) and the AHA (9650529 N). CJB was funded by a graduate fellowship in mathematics and biology at the University of Washington. KEF was funded by an NIH postdoctoral training grant and the AHA.

References

Asada, K., Yoshikawa, K., Takahashi, M., Maeda, Y. & Enmanji, K. (1975). *J. Biol. Chem.* **250**(8), 2801–2807.
Borgstahl, G. E., Pokross, M., Chehab, R., Sekhev, A. & Snell, E. H. (2000). *J. Mol. Biol.* **296**(4), 951–959.
Brünger, A. T. (1993). *X-PLOR Version* 3.1: *A System for X-ray Crystallography and NMR.* New Haven, Connecticut: Yale University Press.
Bunting, K., Cooper, J. B., Badasso, M. O., Tickle, I. J., Newton, M., Wood, S. P., Zhang, Y. & Young, D. (1998). *Eur. J. Biochem.* **251**, 795–803.
Carlioz, A. & Touati, D. (1986). *EMBO J.* **5**(3), 623–630.
Cooper, J. B., McIntyre, K., Badasso, M. O., Wood, S. P., Zhang, Y., Garbe, T. R. & Young, D. (1995). *J. Mol. Biol.* **246**(4), 531–544.
Fridovich, I. (1975). *Annu. Rev. Biochem.* **44**, 147–159.
Fridovich, I. (1995). *Annu. Rev. Biochem.* **64**, 64–112.
Guan, Y., Hickey, M., Borgstahl, G., Hallewell, R., Lepock, J., O'Connor, D., Hsieh, Y., Nick, H., Silverman, D. & Tainer, J. (1998). *Biochemistry*, **37**, 4722–4730.

Hsieh, Y., Guan, Y., Tu, C., Bratt, P., Angerhofer, A., Lepock, J., Hickey, M., Tainer, J., Nick, H. & Silverman, D. (1998). *Biochemistry*, **37**, 4731–4739.
Isobe, T., Fang, Y. I., Muno, D., Okuyama, T., Ohmori, D. & Yamakura, F. (1987). *FEBS Lett.* **223**(1), 92–96.
Keele, B. B. J., McCord, J. M. & Fridovich, I. (1970). *J. Biol. Chem.* **245**(22), 6176–6181.
Kissinger, C. R. & Gehlhaar, D. K. (1997). *EPMR* program. Agouron Pharmaceuticals, La Jolla, California, USA.
Lah, M. S., Dixon, M. M., Pattridge, K. A., Stallings, W. C., Fee, J. A. & Ludwig, M. L. (1995). *Biochemistry*, **34**(5), 1646–1660.
McCord, J. M. (1973). *Oxidases and Related Redox Systems*, pp. 51–76. Baltimore: University Park Press.
McCord, J. M. & Fridovich, I. (1969). *J. Biol. Chem.* **244**(22), 6049–6055.
Marklund, S. L., Holme, E. & Hellner, L. (1982). *Clinica Chim. Acta*, **126**(1), 41–51.
Ose, D. E. & Fridovich, I. (1976). *J. Biol. Chem.* **251**(4), 1217–1218.
Otwinowski, Z. & Minor, W. (1997). *Methods Enzymol.* **276**, 307–326.
Schmidt, M., Meier, B. & Parak, F. (1996). *J. Biol. Inorg. Chem.* **1**(6), 532–541.
Schmidt, M., Scherk, C., Iakovleva, O., Nolting, H. F., Meier, B. & Parak, F. (1998). *Inorg. Chim. Acta*, **276**(1–2), 65–72.
Sines, J., Allison, S. & Wierzbicki, A. (1990). *J. Phys. Chem.* **94**, 959–961.
Sorkin, D. L., Duong, D. K. & Miller, A. F. (1997). *Biochemistry*, **36**, 8202–8208.
Sorkin, D. L. & Miller, A. F. (1997). *Biochemistry*, **36**, 4916–4924.
Stallings, W. C., Powers, T. B., Pattridge, K. A. & Fee, J. A. (1983). *Proc. Natl Acad. Sci. USA*, **80**(13), 3884–3888.
Stoddard, B. L., Howell, P. L., Ringe, D. & Petsko, G. A. (1990). *Biochemistry*, **29**(38), 8885–93.
Stoddard, B. L., Ringe, D. & Petsko, G. A. (1990). *Protein Eng.* **4**(2), 113–119.
Terao, J. & Matsushita, S. (1988). *Free-Radic. Biol. Med.* **4**(4), 205–208.
Valentine, J. S. & Pantoliano, M. W. (1981). *Metal Ions Biol.* **3**, 291–358.
Yamakura, F., Kobayashi, K., Ue, H. & Konno, M. (1995). *Eur. J. Biochem.* **227**, 700–706.
Yamakura, F. & Suzuki, K. (1980). *J. Biochem. (Tokyo)*, **88**(1), 191–196.